Naval Research Laboratory

Washington, DC 20375-5320

NRL/MR/5317--19-9908

Circular Array Beamforming Using Phase Modes

Rashmi Mital
Mark P. Parent
Anna Stumme

Radar Analysis Branch
Radar Division

December 16, 2019

REPORT DOCUMENTATION PAGE

Form Approved
OMB No. 0704-0188

1. REPORT DATE *(DD-MM-YYYY)* 16-12-2019	**2. REPORT TYPE** NRL Memorandum Report	**3. DATES COVERED** *(From - To)* Oct 2018 - July 2019
4. TITLE AND SUBTITLE Circular Array Beamforming Using Phase Modes		**5a. CONTRACT NUMBER**
		5b. GRANT NUMBER
		5c. PROGRAM ELEMENT NUMBER
6. AUTHOR(S) Rashmi Mital, Mark P. Parent, and Anna Stumme		**5d. PROJECT NUMBER** 53-6B48-09-5
		5e. TASK NUMBER
		5f. WORK UNIT NUMBER 6B48
7. PERFORMING ORGANIZATION NAME(S) AND ADDRESS(ES) Naval Research Laboratory, 4555 Overlook Avenue, SW, Washington, DC 20375-5320		**8. PERFORMING ORGANIZATION REPORT NUMBER** NRL/MR/5317--19-9908
9. SPONSORING / MONITORING AGENCY NAME(S) AND ADDRESS(ES) Office of Naval Research, One Liberty Center, 875 N Randolph Street, Suite 1425, Arlington, VA 22203-1995		**10. SPONSOR / MONITOR'S ACRONYM(S)** ONR
		11. SPONSOR / MONITOR'S REPORT NUMBER(S)

12. DISTRIBUTION / AVAILABILITY STATEMENT

DISTRIBUTION STATEMENT A: Approved for public release; distribution is unlimited.

13. SUPPLEMENTARY NOTES

14. ABSTRACT

The desire to perform 360deg horizon surveillance over wide bandwidths has resulted in planar array designs that require multiple faces. Circular/cylindrical phased arrays satisfy many of the stringent requirements on multifunction apertures with their ability to offer full 360deg view using omnidirectional/directional beams. These arrays do not suffer from scan loss or beam broadening. However, cylindrical/circular arrays do have mature beamforming designs like planar arrays. This report provides an overview of one method of transforming circular array beamforming to linear array beamforming allowing use of linear array beamforming techniques. Modeling and simulation efforts to initialize this development is presented.

15. SUBJECT TERMS

Circular array beamforming Phase-modes
180 deg hybrids

16. SECURITY CLASSIFICATION OF:			**17. LIMITATION OF ABSTRACT**	**18. NUMBER OF PAGES**	**19a. NAME OF RESPONSIBLE PERSON** Rashmi Mital
a. REPORT Unclassified Unlimited	**b. ABSTRACT** Unclassified Unlimited	**c. THIS PAGE** Unclassified Unlimited	Unclassified Unlimited	21	**19b. TELEPHONE NUMBER** *(include area code)* (202) 767-2584

Standard Form 298 (Rev. 8-98)
Prescribed by ANSI Std. Z39.18

This page intentionally left blank.

CONTENTS

FIGURES

TABLES

This page intentionally left blank.

EXECUTIVE SUMMARY

The vision of the Navy is to reduce the number of topside masts and the number of single function antennas to help reduce platform signature and acquisition cost. While the desired number of radiating apertures is decreasing the required number of wideband functions is increasing. The desire to perform 360deg horizon surveillance over wide bandwidths has resulted in planar array designs that require multiple faces. Cylindrical/circular phased arrays satisfy many of the stringent requirements placed on multifunction apertures with their ability to offer a full 360deg view using omnidirectional or directional beams. These arrays also do not suffer from scan loss or beam broadening like planar/linear arrays. However, cylindrical/circular arrays do not have mature beamforming designs like planar arrays. This report provides an overview of one method of transforming circular array beamforming to be similar to linear array beamforming such that linear array beamforming methods can be utilized. We present modeling and simulation work that has been done thus far as well as initial test bed development efforts.

This page intentionally left blank.

CIRCULAR ARRAY BEAMFORMING USING PHASE MODES

R. Mital, M. P. Parent and A. Stumme

Radar Analysis Branch, Radar Division

1. INTRODUCTION

The vision of the Navy is to reduce the number of topside masts and the number of single-function antennas to help reduce platform signature and acquisition cost. While the desired number of radiating apertures are decreasing, the required number of wideband functions, such as Radar, Signal Intelligence (SIGINT) and Electronic Warfare (EW) is increasing. The desire to perform 360º horizon surveillance over wide bandwidths has resulted in planar array designs that require multiple faces [1] that have to be overdesigned to compensate for scan loss due to beam steering off broadside.

Cylindrical phased arrays satisfy many of the stringent requirements placed on multifunction apertures because of their ability to offer a full 360º view using either omnidirectional or directional modes without the need for handoff between various faces [2]. Furthermore, unlike planar or linear arrays, cylindrical arrays do not suffer from scan loss as the beam is scanned in the azimuthal direction. Planar arrays need multiple faces to cover the full hemisphere and even then full omnidirectional coverage is not achievable and each planar array is able to cover only a limited scan volume. Cylindrical arrays are able to easily provide full 360º coverage in the azimuthal direction without the need for overdesigning. In the elevation direction, the cylindrical array behaves in the same manner as a planar array. In other words, just as a planar array can be thought of as a product of two linear arrays (see Figure 1a) the cylindrical array is equivalent to a product of a linear array with a circular array (see Figure 1b). Using this simplification in this project, we are only concerned with beamforming techniques for circular arrays and will compare these techniques with the mature beamforming techniques used for linear arrays.

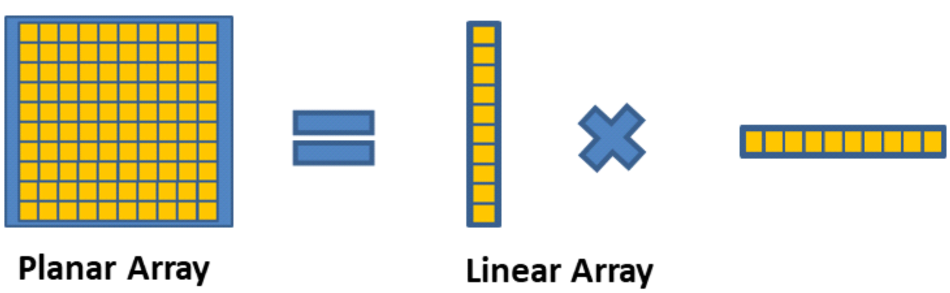

(a)

Manuscript approved November 20, 2019.

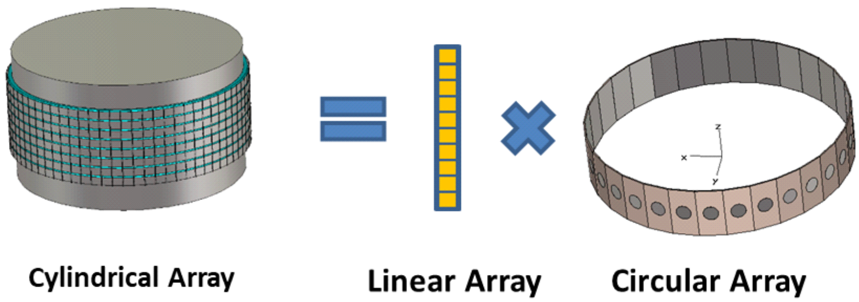

(b)

Figure 1: Simplification of (a) planar array and (b) cylindrical array to a horizontal array and a circular array

1.1 Limitations in Circular Array Beamforming

Figure 2a shows an example of a circular array radiation pattern and compares it to a linear array radiation pattern. Both these arrays are equivalent in length in the azimuthal direction as indicated by the equivalent beamwidth at boresight. The beam in each case is pointing at boresight (i.e. scan angle = 90^o) and the sidelobes are designed to be 30dB from the peak of the main beam. An example of scan loss and the associated beam broadening that occurs in planar and linear arrays is shown in Figure 2b. In this case, the beam points off-boresight at a scan angle of 45^o. The pattern of the circular array looks almost identical to the pattern when the beam was at boresight. There is no beam broadening or scan loss. The pattern from the linear array on the other hand suffers from both beam broadening and scan loss. Thus, the circular arrays are capable of generating radiation patterns with a main beam and sidelobes that are independent of scan angle. Another advantage of using circular arrays is that omnidirectional and sector coverage can be obtained without complex beamforming that is needed when linear or planar arrays are used.

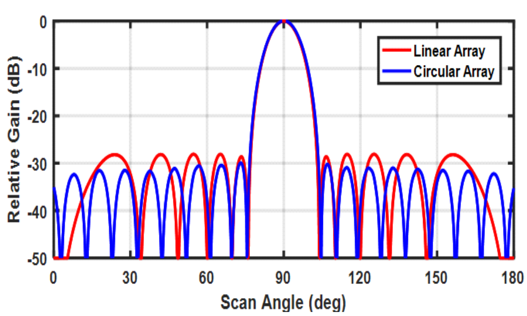

(a)

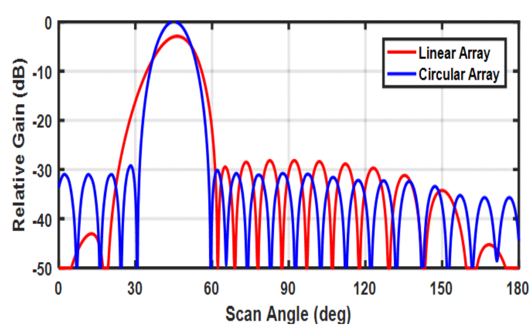

(b)

Figure 2: Beam scanning characteristics in the case when the linear array and circular array are pointing at (a) boresight and (b) 45^o away from boresight. A linear array is affected by beam broadening and scan loss unlike a circular array

Let us look at beamforming for linear and circular arrays to understand the differences between the two cases. The basic linear array has a number of discrete radiating elements, equally oriented and equally spaced, along a straight line as shown in Figure 3.

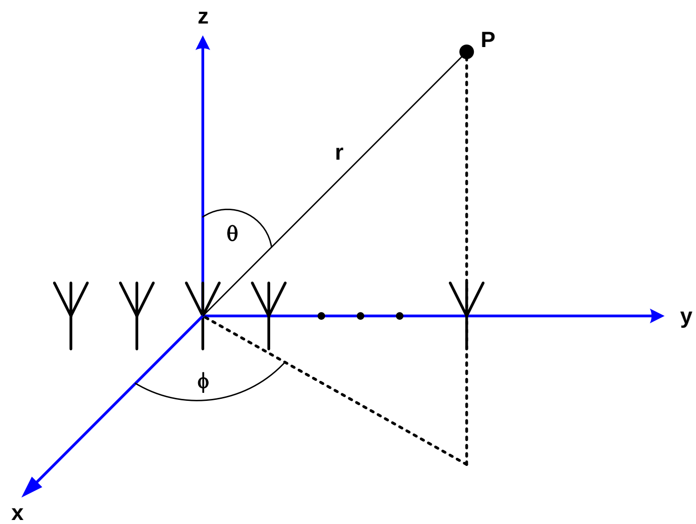

Figure 3: A simple representation of a linear array

The normalized radiation function for one of these elements can be written as $\overline{EL}(\mathbf{r})$ where **r** represents the vector to the far-field point, $\boldsymbol{P}$. The vector **r** is defined in terms of range, azimuth angle, ϕ, and elevation angle, θ. If the complex excitation at element n is ω_n and its element pattern is $EL_n(r, \theta, \phi)$, then summing over all the elements in the linear array gives the overall radiation pattern as

$$\overline{E}(\mathbf{r}) = \sum_n \omega_n \overline{EL}(\mathbf{r} - \mathbf{r_p}) e^{-jk|\mathrm{r}-\mathrm{r}_p|}. \tag{1}$$

In the far-field, the dependence on the distance is approximately the same for all radiating elements and further, it can also be assumed that all the elements populating the linear array are identical. This assumption allows us to extract the element's radiating factor outside the summation. It is now referred to as the element factor and the summation is referred to as the array factor. Since the distance from each of the elements in the array to the point, $\boldsymbol{P}$, is about the same, the term r can be discarded and the radiating factor now only has dependence on (θ, ϕ). This representation is shown in Eq. (2).

$$\overline{E}(\theta, \phi) = \overline{EL}(\theta, \phi) \times AF(\theta, \phi). \tag{2}$$

For linear and planar arrays, the array factor plays a significant role. The element factor normally can be approximated by a cosine pattern and does not have significant effects on the overall pattern. For linear arrays, the array factor can be simplified to just the radiation in the azimuthal plane as shown in Eq. (3).

$$E(\phi) = EL(\phi) \times \sum_n \omega_n e^{jknd\cos\phi} \tag{3}$$

Now let us look at the circular array radiation pattern. In this array, the elements are equally spaced along the periphery of the circular array as shown in Figure 4.

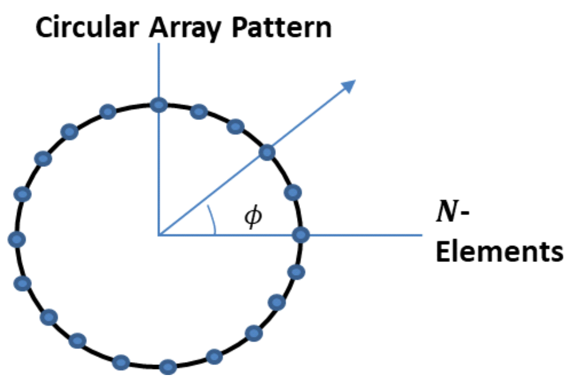

Figure 4: A representation of a simple circular array. The main beam is in the plane of the array. The elements radiate in the radial direction and are related to one another by a fixed rotation angle.

Once again, we are interested only in the radiation in the azimuthal plane. With this assumption, the expression for the far-field radiation pattern can be written in the form shown in Eq. (4).

$$E(\phi) = \sum_n \omega_n EL(\phi - n\Delta\phi) e^{jkR\cos(\phi - n\Delta\phi)} \tag{4}$$

The phase in this equation is referenced to the center of the circle of radius R. The elements are spaced $R\Delta\phi$ along the circle with each element pointing in the radial direction. Note that in the circular array radiation pattern the element function cannot be brought outside the summation as it changes element to element making the element pattern unique for each radial direction. Thus, the radiation pattern for a circular array cannot be defined as a product of the element factor and an array factor as for a linear array.

The uniqueness of the elements in the circular array results in a complex synthesis of array tapers and beam steering weights for synthesizing of directional beams. Each time the scan angle or frequency of operation changes, the weights applied at the elements need to be re-calculated. This makes circular array beamforming challenging and impractical. This is one of the reasons why circular arrays are not as widely used as linear arrays even though there are many advantages to using them.

The rotational relationship means that each element in the circular array has a unique embedded element pattern resulting in a complex synthesis of array tapers and beam steering weights for directional beams. Each time the scan angle or frequency of operation changes for a circular array, the weights applied at the elements must be recalculated. In other words, the weights applied to the elements have to be optimized for every scan angle and frequency that the circular array operates, making the design of circular array challenging. This is one of the reasons why circular arrays are not as widely-used as linear arrays even though there are advantages to using them.

Equation (3) states the far-field expression for a linear array essentially shows a Fourier relationship between the far-field pattern and the complex excitation. However, the circular array expression does not show this relationship. If a similar Fourier relationship could be obtained for circular array beamforming, it is possible to make circular array beamforming less complex. To achieve this, we plan to use phase mode theory [3, 4].

Phase modes can be considered to be similar to elements of a linear array and thus their use will allow mature linear array techniques to be used for beamforming. Analog or digital techniques can be used for these transformations. In this project, we are interested in investigating analog techniques which can use a Rottman lens [5] or Butler matrices. Butler matrices have the capability of providing a flat phase shift across a wider frequency thus allowing wideband beamforming unlike the Rottman lens method. An example of the phase shift vs. frequency is shown in Figure 5. Phase variation is shown from input 1 to four of the outputs. When a Butler Matrix is implemented, the phase change remains constant across the frequency, as indicated by the constant lines, however, when another network such as a Rottman Lens is used, the phase varies across frequency providing the correct phase at only one of the frequencies, in this case that is at 4.5 GHz. This is the reason why a Butler Matrix network is more suited to form phase modes from circular array elements.

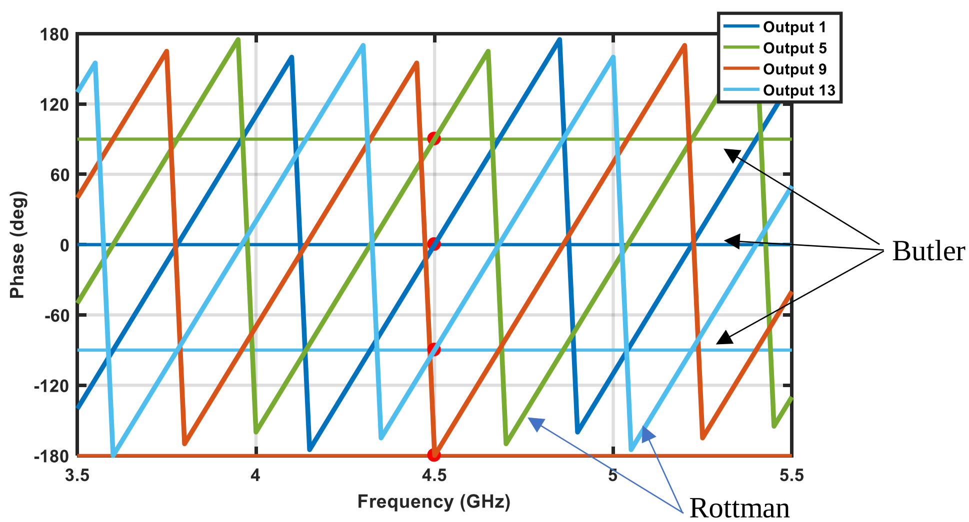

Figure 5: Phase change across frequency when using a Butler Matrix and a Rottman Lens

In this report, we will discuss how circular array elements can be transformed into phase modes using the Butler matrix hardware. We will also touch on hardware errors and how these effect overall beam patterns.

2. PHASE MODES

2.1 Forming Phase Modes

As mentioned earlier, the steering vector of a uniform circular array does not have progressive phase across the elements as does a linear array, which means that the simplification of calculating the radiation pattern as the product of an average element radiation pattern and the array factor cannot be used. Instead, we plan to use phase mode theory [3-4,6-7]. In this section, a short overview of phase modes is provided.

To explain phase modes, let us look at the case when the excitation on a circular array is continuous [6]. For this case, the far-field pattern in the azimuthal plane can be written in terms of complex excitation ω_n and the element radiation pattern, EL, as shown in Eq. (5).

$$E(\phi) = \frac{1}{2\pi} \int_{-\pi}^{\pi} \omega(\varphi)\, EL(\phi - \varphi) e^{jkR\cos(\phi - \varphi)}\, d\varphi \tag{5}$$

The excitation function is periodic over 2π so it can be expanded using Fourier theory for a periodic function as

$$\omega(\varphi) = \sum_{-\infty}^{\infty} C_m e^{jm\varphi}. \tag{6}$$

Or its inverse as

$$C_m = \int_{-\pi}^{\pi} \omega(\varphi) e^{-jm\varphi} d\varphi. \tag{7}$$

Each coefficient, C_m, represents the excitation needed to generate a phase mode. When $m = 0$, this represents the 1st mode that has no phase variation along the circumference of a circular array. In a similar vein, the m^{th} mode has $m \times 2\pi$ variations along the circumference. The value of m can be positive or negative. An example of phase modes is shown in Figure 6. In this figure, the phase of three different phase modes is shown: the 0th mode, 1st mode and 2nd mode. Note that the number of phase variations equals the mode number. Not shown, but if the mode number is negative, the slope will vary in the other direction.

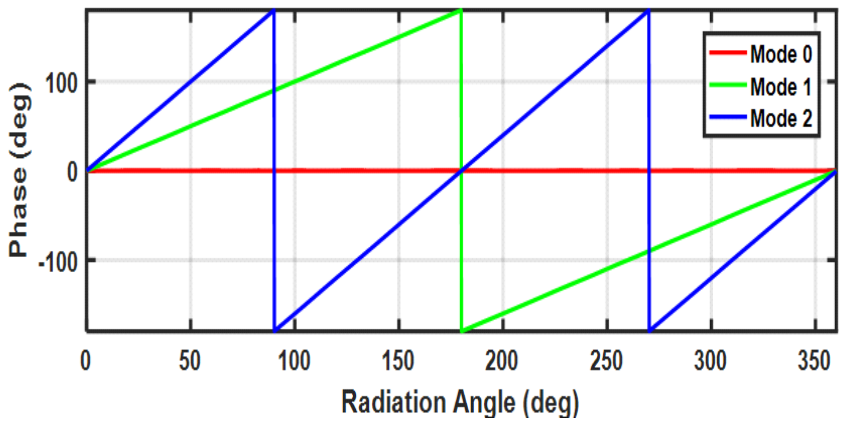

Figure 6: Examples of phase variation of modes vs. radiation angle

Looking at the example where the elements populating the circular array are isotropic in nature, the far-field radiation pattern can be written in terms of the phase mode excitations as

$$E(\phi) = \frac{1}{2\pi} \int_{-\pi}^{\pi} \sum_{-\infty}^{\infty} C_m e^{jm\varphi} e^{jkR\cos(\phi-\varphi)} d\varphi. \tag{8}$$

Reversing the order of integration and summation yields

$$E(\phi) = \sum_{-\infty}^{\infty} C_m \frac{1}{2\pi} \int_{-\pi}^{\pi} e^{jm\varphi} e^{jkR\cos(\phi-\varphi)} d\varphi\,. \tag{9}$$

As the far-field function is also periodic if the applied excitation is periodic, it can also be represented as a Fourier series as shown in Eq. (10).

$$E(\phi) = \sum_{-\infty}^{\infty} A_m e^{jm\phi} \tag{10}$$

Comparing the two expressions for the far-field radiation pattern and removing the summation sign,

$$A_m = C_m \frac{1}{2\pi} \int_{-\pi}^{\pi} e^{-jm(\phi-\varphi)} e^{jkR\cos(\phi-\varphi)} d\varphi \tag{11}$$

Thus, the far-field phase mode amplitude $A_m$is related to the excitation terms, C_m through Eq. (11) which is an integral representation of the Bessel function of the first kind [6]. Note, when the far-field radiation pattern is expressed as a summation of phase modes as shown in Eq. (10), it has a progressive phase shift analogous to the linear array factor. Thus using phase mode transformation, it is possible to describe circular array radiation patterns in a similar manner as for a linear array.

The discrete array excitation can be thought of as a sampled version of the continuous case. In this case, feeding the elements with a linear increasing phase will provide the desired phase modes but it also results in the generation of harmonics to the fundamental phase mode, which can result in additional radiation modes. These are often referred to as "distortion modes" [6]. These distortion modes limit how many modes can be used for beamforming. These are discussed later in this report.

Finally, if the radiating elements are directive instead of isotropic, this effect also needs to be included into the expression of the phase modes. The element radiation pattern will also be periodic over 2π and can be written as a Fourier series.

$$EL(\alpha) = \sum_{p=-\infty}^{\infty} D_p e^{jp\alpha} \tag{12}$$

Inserting Eq. (12) into the far-field radiation pattern, Eq. (5), the far-field radiation can be written as

$$E(\phi) = \frac{1}{2\pi} \int_{-\pi}^{\pi} \omega(\varphi) \sum_{p=-\infty}^{\infty} D_p e^{jp(\phi-\varphi)} e^{jkR\cos(\phi-\varphi)} d\varphi. \tag{13}$$

Expanding the excitation term, each phase mode term can be written as a ***product*** of two terms as shown in Eq. (14).

$$E_m(\phi) = C_m e^{jm\phi} \sum_{p=-\infty}^{\infty} D_p \frac{1}{2\pi} \int_{-\pi}^{\pi} e^{-j(m-p)(\phi-\varphi)} e^{jkR\cos(\phi-\varphi)} d\varphi \tag{14}$$

Eq. (14) shows the phase modes for continuous excitation. For a circular array with discrete elements, the phase modes can be calculated using Eq. (15). The phase, φ, is replaced by the rotation angle of the elements in the array.

$$A_m(\phi) = \sum_{p=1}^{N} D_0\left(\phi - \frac{2\pi p}{N}\right) e^{jm\left(\phi-\frac{2\pi p}{N}\right)} e^{jkR\cos\left(\phi-\frac{2\pi p}{N}\right)} \tag{15}$$

The final radiation pattern can then be provided by summing all the phase modes. For each phase mode, the contribution of all the element radiation patterns has to be included. In this report, we look into the effect of the element radiation pattern variation on the phase mode excitation, A_m, including the frequency variation. Reference [6] discusses how an actual element pattern's Fourier representation affects the phase modes.

As mentioned earlier, a Butler matrix connected to circular array elements is able to create a linear phase variation among the elements as desired from the equations earlier. For example an $N \times N$ Butler matrix can be used to excite at least N independent phase modes, each radiating an omnidirectional amplitude pattern but with different phase variations. Shelag [7] and Steyskal [3] discussed how Butler matrices can be used to form phase modes. After equalization, a second set of complex weights can be added, as shown in Figure 7, to form the desired directional beams. We represent the Butler matrix and equalization as a "modal beamformer" as its purpose is to form phase modes. A circular array with N elements will form N phase modes and a subset of these modes can be weighted to form directional modes.

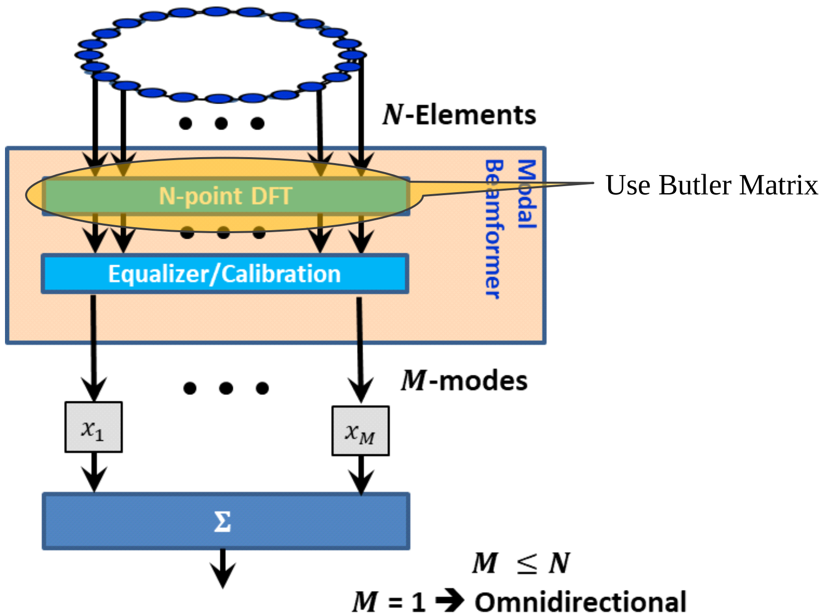

Figure 7: Modal Beamforming to form phase modes from circular array elements

2.2 Butler Matrix

A Butler Matrix is a beamforming network commonly used in phased array antennas to form multiple directional beams with each beam pointing in a different direction. A standard Butler matrix is denoted as a network with N as the number of input and output ports. An input to port n of the Butler Matrix provides a progressive phase shift across the output ports. This network consists of hybrid couplers and fixed value phase shifters. The Butler matrix feeds elements of a linear array with a progressive phase difference such that the combined beam points in a desired direction. The direction of the beam can be controlled by switching to the different output ports. An N-port Butler matrix provides the capability to transmit or receive up to N simultaneous beams.

The Butler matrix is a passive reciprocal device, which means that it operates the same regardless of whether it is used to transmit or receive. An example of a 4×4 Butler matrix is shown in Figure 8.

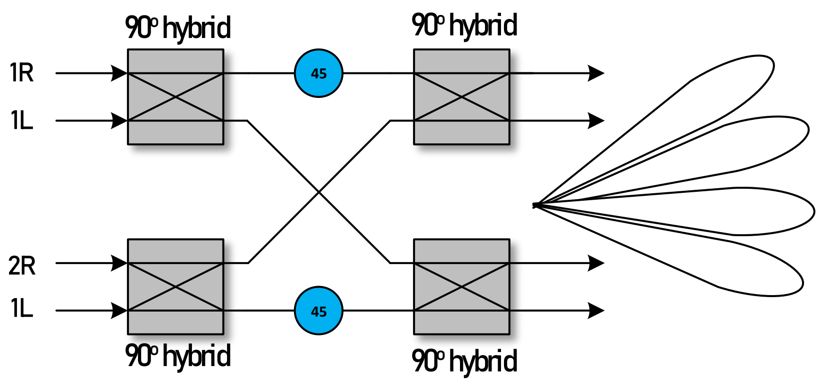

Figure 8: A representation of a 4 × 4 Butler matrix

A Butler matrix can also feed a circular array [3,6]. When the inputs to the network are circular array elements, the outputs are a set of orthogonal phase modes. These orthogonal phase modes all have the same amplitude but have phase that cycles a different number of times (see Figure 6). These phase modes can now be considered as "linear elements" and linear array beamforming techniques can be used.

Butler matrices are conventionally designed using 90° hybrids as shown in Figure 8. When this is the case, the resultant set of beams form symmetrically about the center. However, in Ref [8], it is shown that by using 180° hybrids instead, the direction of the beams are asymmetrical with a radiating beam at the ϕ = 0° as well. When using circular arrays as the input, using 180° hybrids allows the formation of the 0th order phase mode. Another advantage with the 180° hybrid design is the reduction in the number of phase shifters needed. For example, in a 4 × 4 design the number of phase shifters reduces from two to one when 180° hybrids are used.

A typical 180° hybrid is shown in Figure 9 [8]. In this hybrid, input at port 1 produces equal outputs at port 2 and 3 with these outputs being out of phase by 180°. When the incoming signal is at port 4 then the outputs at ports 2 and 3 are equal both in amplitude and phase.

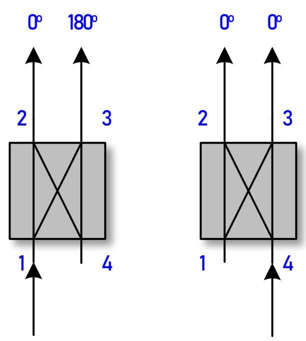

Figure 9: A typical 180° hybrid

The performance of a commercially available hybrid was modeled using Keysight's GENESYS tool. The Werlatone Model H10126 is a surface mount hybrid operating from 2 – 6 GHz and capable of handling 100 W continuous power (CW). The port-to-port isolation is stated to be 20 dB. Figure 10a shows the simulated performance of this component. Figure 10b shows the phase response at the outputs 2 and 3. As expected, when the signal is fed at Port 1, the output ports have a phase difference of 180^o, and when the signal is fed into Port 4, the output signals have no difference. The input signal is equally divided at the output regardless of which input is fed, which is why the S_{21} , represented by S_{12} and S_{13} shows loss greater than 3dB.

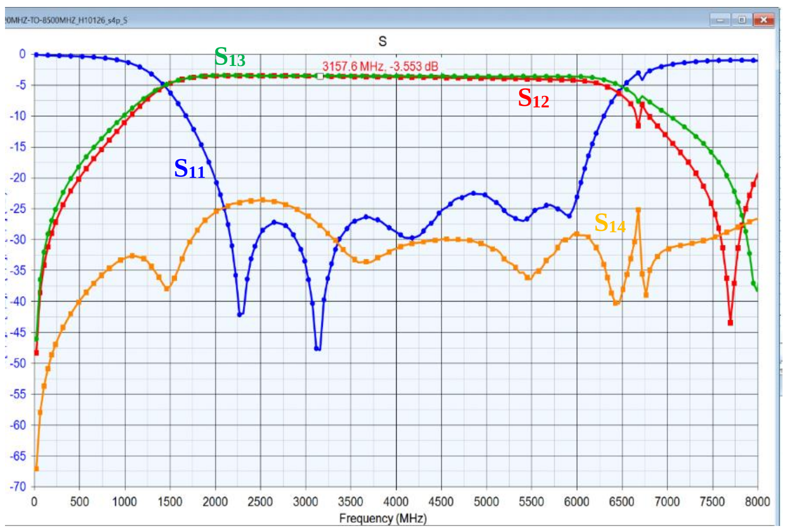

(a)

	F (MHz)	ang(S[1,2])-ang(S[1,2]) (°)	ang(S[1,3])-ang(S[1,2]) (°)	ang(S[4,2])-ang(S[4,2]) (°)	ang(S[4,3])-ang(S[4,2]) (°)
1	4000	0	180.528	0	0.644
2	4200	0	180.789	0	0.907
3	4400	0	180.966	0	1.108
4	4600	0	181.132	0	1.316
5	4800	0	-178.706	0	1.635
6	5000	0	-178.355	0	2.053
7	5200	0	-178.029	0	2.394
8	5400	0	-177.767	0	2.669
9	5600	0	182.595	0	3.062
10	5800	0	183.267	0	3.659
11	6000	0	183.918	0	4.483

(b)

Figure 10: (a) Modeled S-parameter performance of Werlatone H10126 hybrid. (b) Snapshot of the phase performance at the outputs of the 180^o hybrid

The error from 180^o and 0^o for this hybrid is shown in Figure 11. The errors in phase increase with increasing frequency. The worst case error is about 3^o at 5500 MHz.

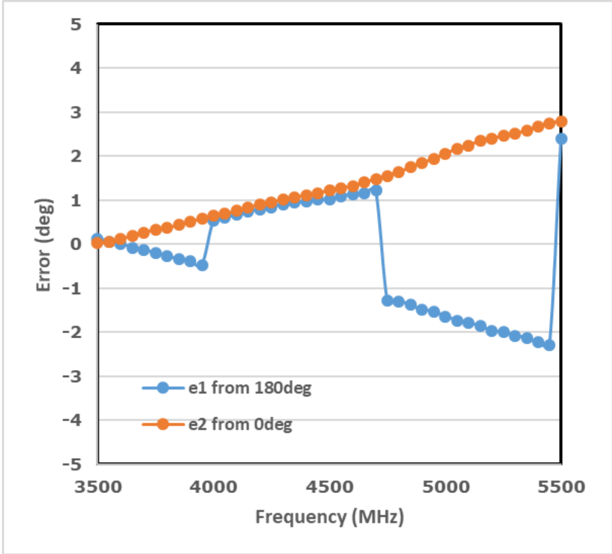

Figure 11: Error in Phase at the output of Werlatone H10126 hybrid

In future studies, analysis will be done to quantify how the phase errors in the hybrids, as well as the phase shifters, are translated into the overall performance of the Butler Matrix. In the next section, we will look at how to design a Butler Matrix.

2.3 Designing a Butler Matrix

Using Ref [8], we were able to completely design a Butler Matrix following a fixed set of rules. Each of these will be discussed in turn.

2.3.1 Number of Hybrids

The number of hybrids for a design can be determined using the formula

$$N_{Hybrids} = \frac{Nn}{2} \tag{16}$$

where the relationship between the number of inputs/outputs, N, and the number of rows, n, can be determined by $N = 2^n$. Thus when designing a 4×4 Butler matrix, the number of hybrids is 4 (as seen in Figure 8). Table 1 determines the number of hybrids for other cases. These hybrids are arranged in n rows each with $\frac{N}{2}$ hybrids.

Table 1: Number of hybrids vs. size of Butler Matrix

Number of Inputs / Output (N)	$N_{Hybrids}$
8	$3 \times \frac{8}{2} = 12$
16	$4 \times \frac{16}{2} = 32$
32	$5 \times \frac{32}{2} = 80$
64	$6 \times \frac{64}{2} = 196$

2.3.2 Number of Phase Shifters

The next important component needed in the network is the fixed phase shifter. The term "fixed" indicates that the phase shifter needs to be frequency invariant over the band of operation of the Butler Matrix as shown in Figure 5. In other words, the phase should not vary across the band. This is the functionality of the Butler matrix that makes it ideal for the formation of phase modes from the circular array elements. Networks such as Rottman lens are unable to provide this "fixed" phase shift and instead provide a constant time delay across the frequency range resulting in a changing phase shift as shown in Figure 5. However, this also means that we need a flat phase shift response across the band of operation. We will address this issue in a later report.

For an 8 port Butler matrix, the number of rows with phase shifters will be 2. For Butler matrices using the 180^{o} hybrids, the number of hybrids in each row can be determined by Eq. (17)

$$N_{PhaseShifters} = \frac{N}{2} - 2^{k-1} \tag{17}$$

Where k is the row number and it is defined as the row closest to the output port. Table 2 shows the exact number of phase shifters needed for different sized networks. For a 16×16 network, there will be 3 rows of phase shifters with a total of 17 phase shifters needed.

Table 2: Number of fixed phase shifters for each row for Butler Matrices of different sizes. “0” s indicate that row is not available.

Row Number k	N = 4	N = 8	N = 16	N = 32
1	1	3	7	15
2	0	2	6	14
3	0	0	4	12
4	0	0	0	0
5	0	0	0	0
6	0	0	0	0

2.3.3 Position and Magnitude of Fixed Phase Shifters

The final step for completing the full design of a Butler Matrix is to determine the positions and magnitude of fixed phase shifters. Once again, using the equations and discussions of Ref. [8], we were able to determine the relevant details for the design. As it turns out, the phase shifters added only onto the odd sections (i.e., 1st, 3rd, 5th and so on) of the design and phase difference between the two output ports is a fixed value of 90^{o}. Finally the difference between every other port 2 of the odd section can be determined by $\frac{360^0}{N} \times 2^{k-1}$. Using these set of rules, the designs of an 8×8 and a 16×16 Butler Matrix are shown in Figure 12.

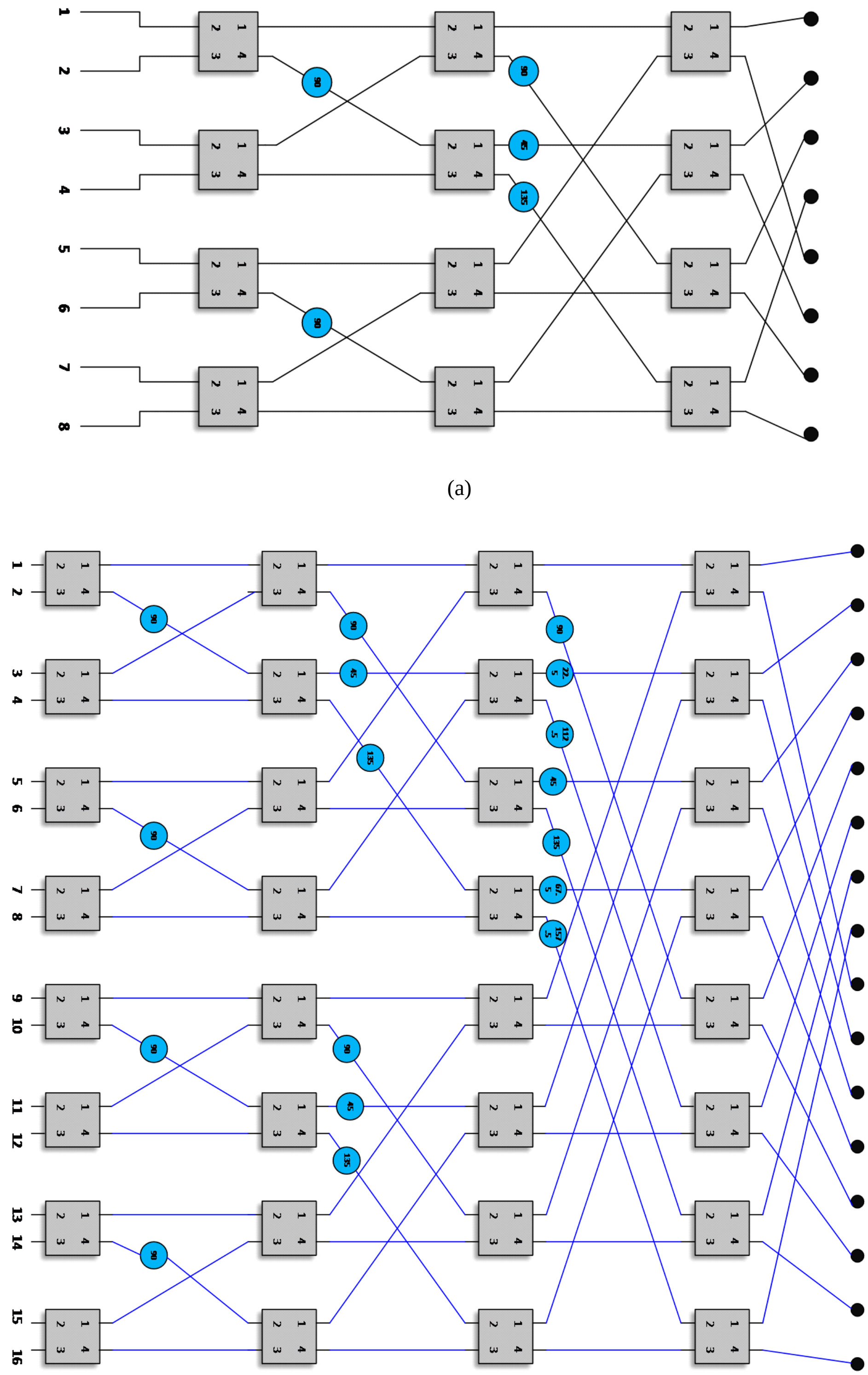

(a)

(b)

Figure 12: Designs for (a) an 8×8 and (b) a 16×16 Butler Matrix using the design concepts discussed earlier. The Butler networks consist of 180^o hybrids and fixed phase shifters [8].

As mentioned before, when the elements of a circular array are connected to the input of the above Butler Matrix design, it is possible to excite simultaneously and independently all the desired phase modes at the output. In the next section, a discussion of the simulation results is provided.

3. MODELING EFFORTS

In this section, we discuss the modeling and simulation efforts to verify the performance of Butler Matrices to form phase modes from circular array elements. To start this effort, the first step is to design and simulate an actual circular array that can be used as the input to the Butler Matrix. For this project, we have chosen to build hardware for a 16-element circular array. Larger arrays require networks with too many components while smaller designs have been studied in the literature and do not provide sufficient learning experience. From Table 1 and 2, a 16-input network will require 32 hybrids and 17 fixed phase shifters with 7 unique phase shift values.

3.1 Circular Array

The circular array designed for this effort follows the design provided in Ref [9]. It uses a stepped notch antenna element designed to operate from 3 – 6 GHz. This array was manufactured using metal Plating on Plastic (PoP) 3-D printing. The complete circular array was manufactured as a solid piece using selective laser sintering printing that provided high-precision printing without the need for difficult to remove external supports. After printing, the array is electroplated with copper to effectively become an all metal radiator. This circular array design (shown in Figure 13) has an outer diameter of 5.0 in and a height of 1.2 in.

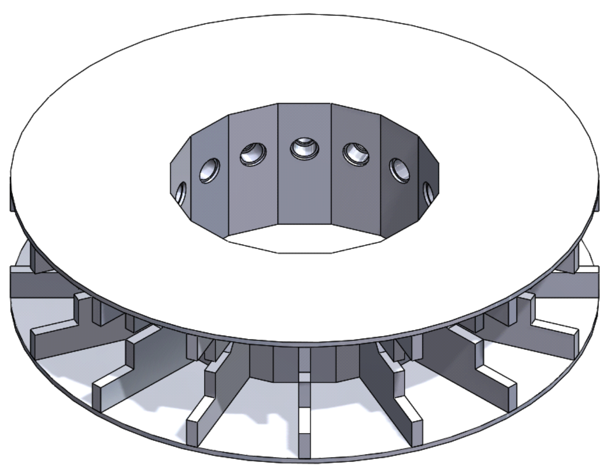

Figure 13: Illustration of the 16-element 3-D printed circular array

Simulating a circular array is a demanding process due to the unconventional boundary conditions needed to simulate a unit cell. Once again, the rotational relationship between the individual elements makes the simulation complex and time consuming. A detailed discussion of how a combination of unit cell and circular array geometry can be used to analyze and model circular arrays is provided in Ref [10]. The unit cell for this circular array is shown in Figure 14.

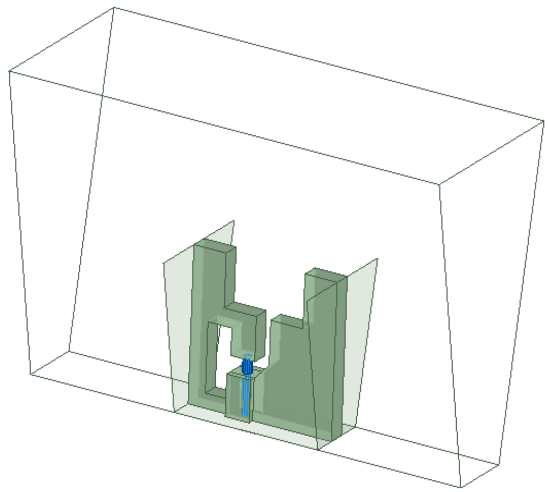

Figure 14: Unit cell and wedge boundary definitions for a circular array unit cell

Ref [10] provides a discussion is provided of how the radiation pattern is computed from a periodic unit cell (as shown in Figure 14) is not sufficient and does not provide a complete model of the element radiation pattern. To determine this, the pattern of the full array is simulated with only a single element excited and the rest of the elements terminated. The resultant pattern is referred to as the embedded element pattern. The embedded element pattern properly accounts for mutual coupling effects and is unique for each element in the array. It may differ based on its location in the array. However in a circular array, the embedded element pattern for each element is related by a rotation. An example of an embedded element pattern for the array of Figure 13 is shown in Figure 15. The pattern is shown for several different frequencies over the operational band of the array. In this example, the embedded element is of an element pointing at boresight.

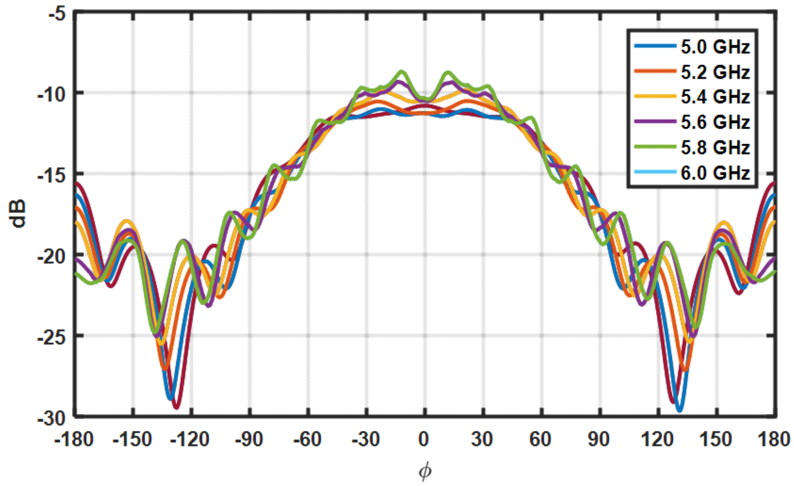

Figure 15: Embedded element pattern for one of the elements in the 16-element circular array

3.2 Modeling Butler Matrix

The 16×16 Butler matrix was simulated in Keysight's GENESYS tool. The layout of this network as modeled in GENESYS is shown in Figure 16. The GENESYS tool does not have a 180^{o}-hybrid so this part was modeled as a 4-port S-parameter data block as shown in Figure 17. The input ports are 1 and 4 and the output ports are 2 and 3. A touchstone file format was used to enable GENESYS to read in the measured S-parameter data of the hybrid. For now, this data was provided by the vendor.

In the next section, we analyze the results from this simulation and form actual beam patterns comparing performance from an ideal network to a network using non-ideal components.

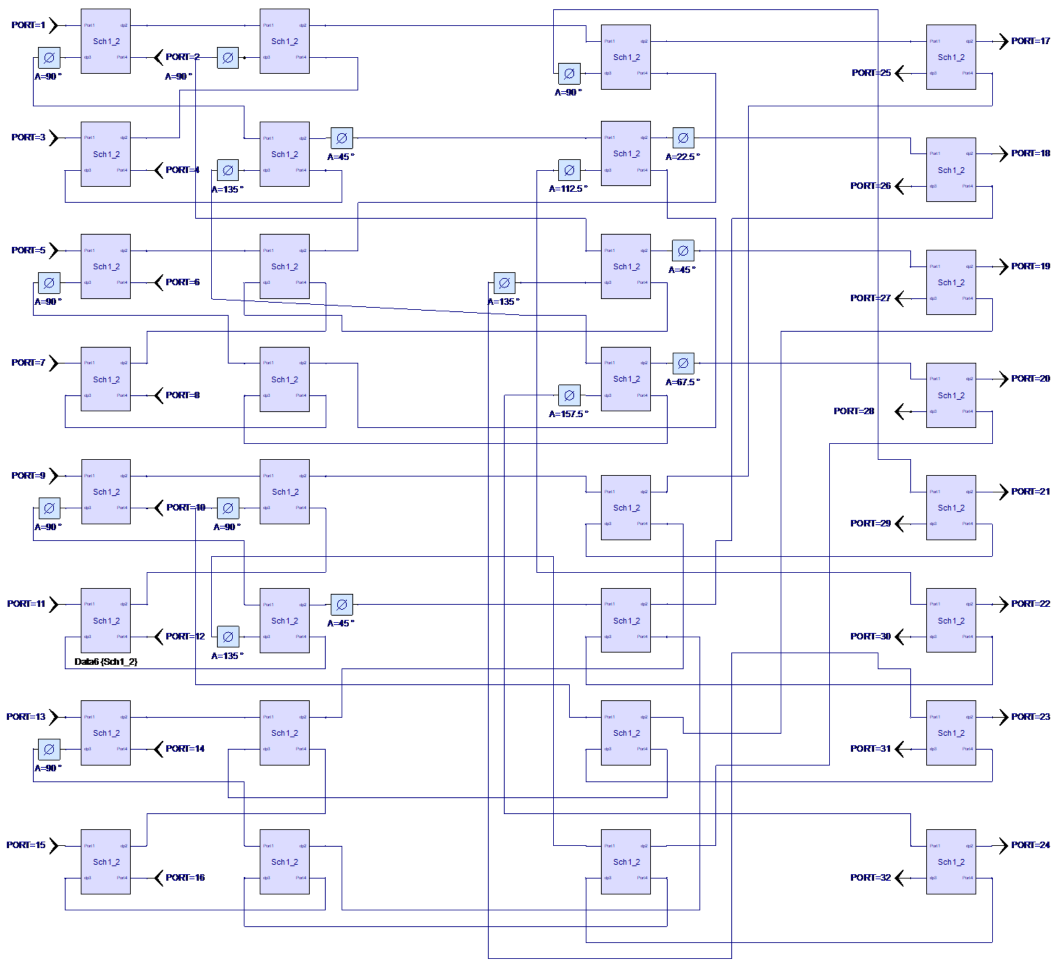

Figure 16: Representation of a Butler Matrix as modeled in GENESYS

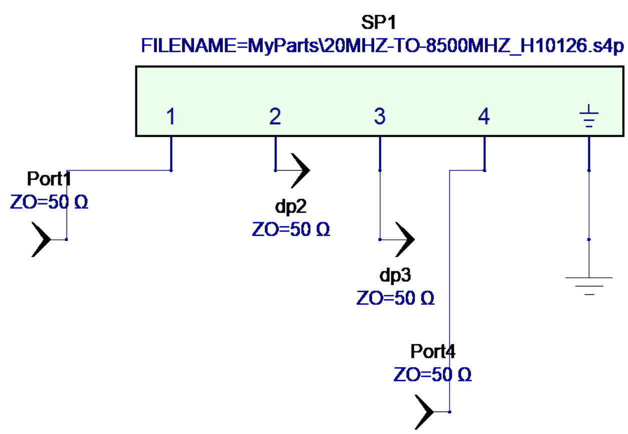

Figure 17: 4-port S-parameter data block to model an 180deg hybrid

4. RESULTS

In this section, we look at the results of the models and show that we are able to form the phase modes using the designed 16-port Butler Matrix. Using the 16-port network in Figure 16, it was possible to simulate a 32×32 S-matrix using GENESYS. For this analysis, only a subset of this matrix is of interest; the set that relates the output ports (17 – 32) to the input ports (1 – 16). Once this subset was extracted a simple matrix multiplication of the S-matrix with a matrix made of rotated embedded elements, can be employed to form all 16 phase modes. Table 3 shows which phase mode is created at which output. For example, the 0^{th} phase mode is generated at port 32 while the 1^{st} phase mode is formed at port 25.

Table 3: Output port at which n^{th} phase mode is created for a 16-port Butler Matrix

Phase Mode	Output Port
-7	18
-6	26
-5	22
-4	30
-3	20
-2	28
-1	24
0	32
1	17
2	25
3	21
4	29
5	19
6	27
7	23
8	31

Figure 18 shows these phases in graphical form comparing the ideal (in "blue") phases to the simulated phases (in "red"). All plots have the y-axis ranging from -180^{o} to +180^{o}. Note that the number of times the phase cycles between the minimum and maximum range is based on the phase number. Also the slope direction changes for positive and negative phase modes.

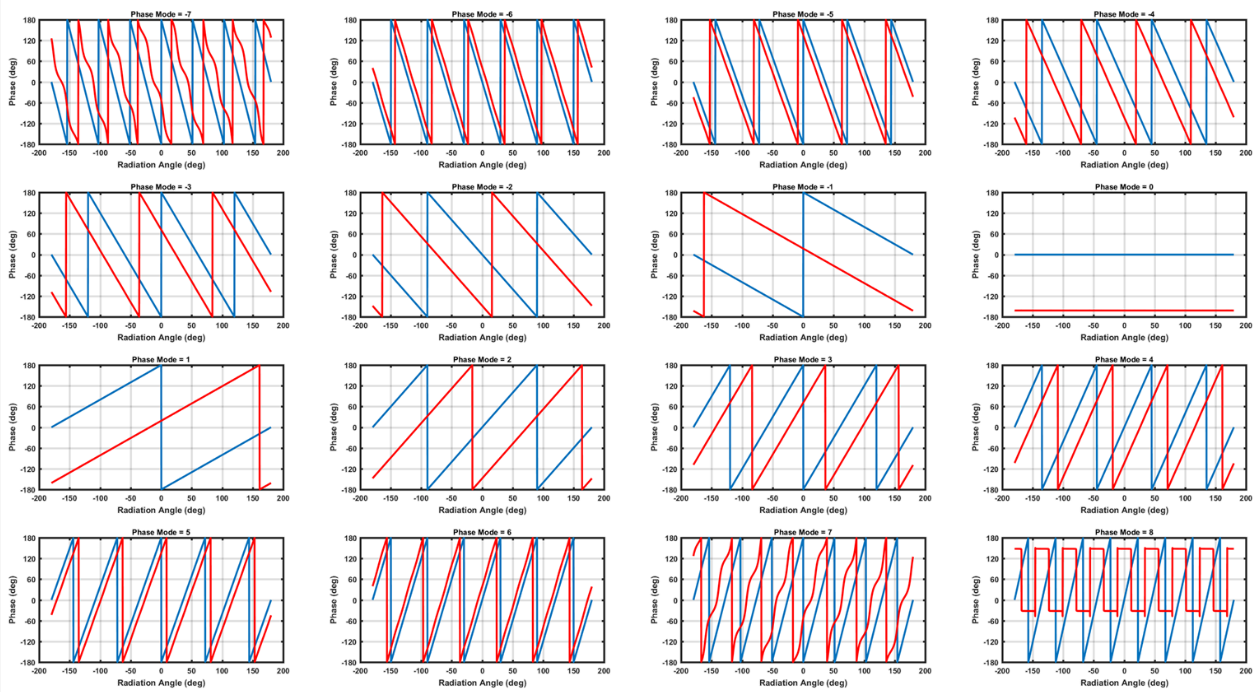

Figure 18: Phase Variation of the 16 Phase Modes formed using a 16-port Butler Matrix

Another point to note in these results is that the ideal and the simulated do not lie exactly on top of one another. The two patterns start at different phases and this phase difference varies from phase mode to phase mode. The difference in this phase is plotted in Figure 19. This difference is a result of the Fourier coefficient of the embedded element pattern. Also, this difference will vary frequency to frequency because there are variations in the embedded element pattern across the frequency band as seen in Figure 15. These differences need to be equalized across modes and frequency band.

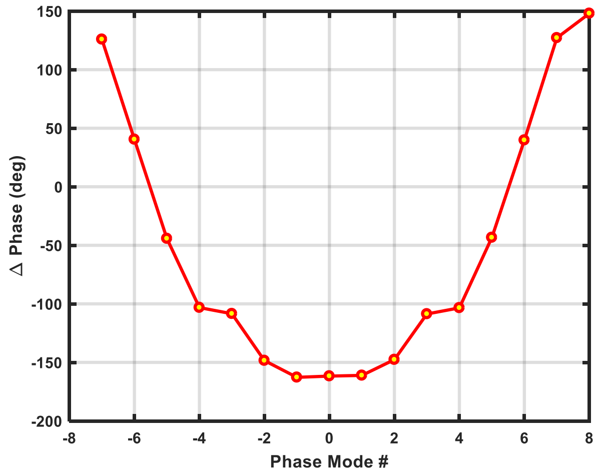

Figure 19: Phase difference between simulated and ideal phase modes

If the phase modes are added together without any equalization of the phase, the resultant sum will equal the embedded element pattern as shown in Figure 19 and discussed in Ref [11]. Later we will show how errors in the hardware affect this calculation.

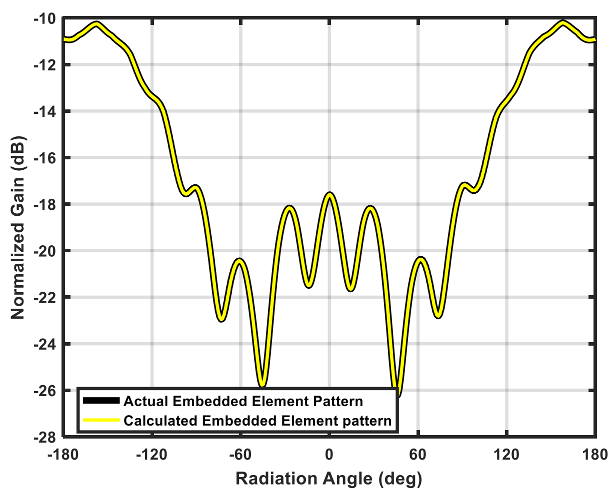

Figure 20: Calculating embedded element pattern from phase modes

Once the equalized phase shifts are added at the output of the Butler matrix, the phase difference between the ideal and simulated phase modes is removed resulting in the modification of Figure 18 to Figure 21. There are some errors in the higher order modes but the lower order modes match the ideal phase modes perfectly. The errors in the higher order modes can be explained by distortion errors [6] however these modes do not typically get used at lower frequencies.

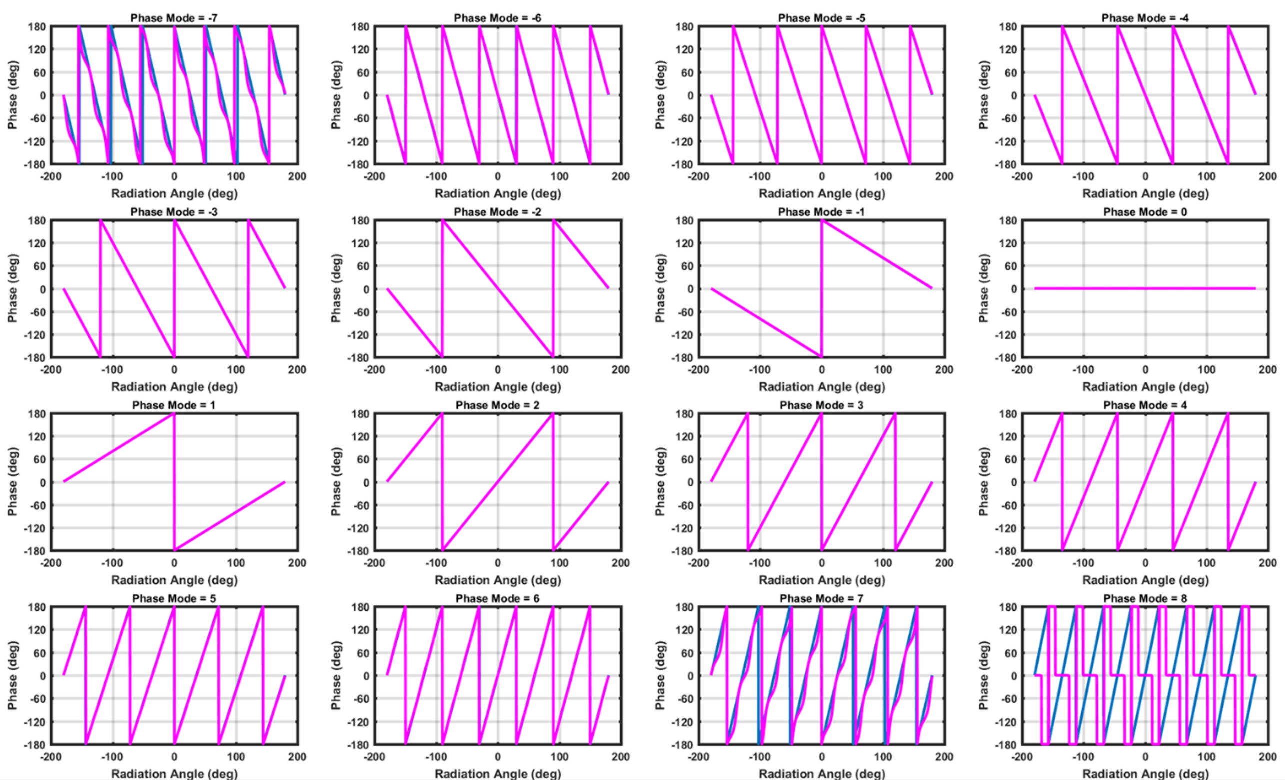

Figure 21: After equalization, simulated and ideal phase modes are the same

Adding the equalized phase modes together will give a directional pattern as shown in Figure 22. The beamwidth is dependent on the number of phase modes that are added together. The larger the number of phase modes the narrower the beam; equivalent to what happens in a linear array. An example of a directive pattern pointing boresight and at an off-boresight angle is shown in Figure 22. Note that the boresight and scanned beams have the same gain and there is no beam-broadening or scan loss.

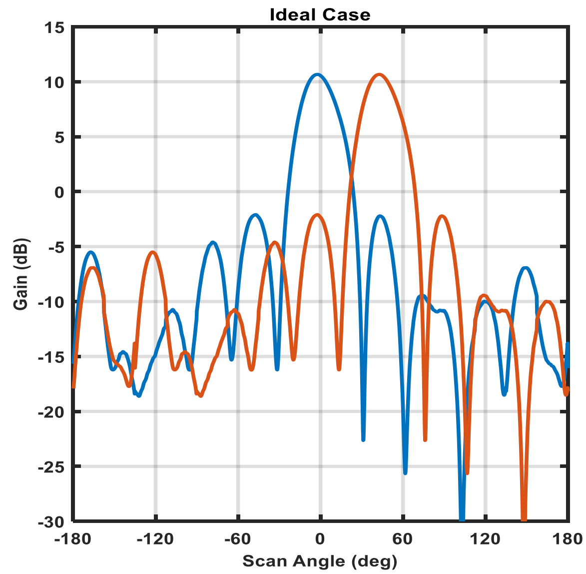

Figure 22: Example of directive beam formed by summing equalized phase modes

The results presented so far assume the use of ideal hybrids, phase shifters and antenna element designs so the equalization errors are present due to the discrete Fourier coefficients of the embedded element patterns. Next, let us look at how equalization errors are affected by the use of non-ideal components. In the next set of presented results, we simulate the 16-port Butler matrix using the COTS 180^{o} hybrid and measured embedded element patterns. For now the phase shifters are still assumed to be ideal, i.e. they provide a flat, fixed phase shift across the band of operation. We are currently looking into the designs of these phase shifters. These will be presented in a future report.

Figure 23 shows the measured active reflection coefficient vs. phase modes for frequencies ranging from 3 GHz to 6 GHz. From the plot, it can be seen that mode 0 is well-matched (i.e. active reflection coefficient is better than -10dB) across the entire band. However, as we look at the higher modes, these are only matched at the higher frequencies. Theory [6] shows that higher order modes do not radiate well. Modes of order $|m| > \frac{2\pi}{\lambda}R$, where R is the radius of the array, should be avoided as these decay in amplitude rapidly and therefore do not radiate well [6]. In the case when the elements are spaced $\frac{\lambda}{2}$ the number of modes that will radiate well follows the requirement $|m| < \frac{N}{2}$. However, if the spacing is further reduced then the number of modes reduce. For example, if the elements are now placed $\frac{\lambda}{8}$ apart, only $|m| < \frac{N}{8}$ will radiate well. The higher order modes will act as distortion modes. This limit is represented by the "white" lines in Figure 23.

For the remaining analysis, we looked at a narrower frequency range, choosing 4.35 – 4.7 GHz as the 180° hybrid has small phase errors at this frequency range and the circular array element were well matched (i.e. reflection is better than 2:1).

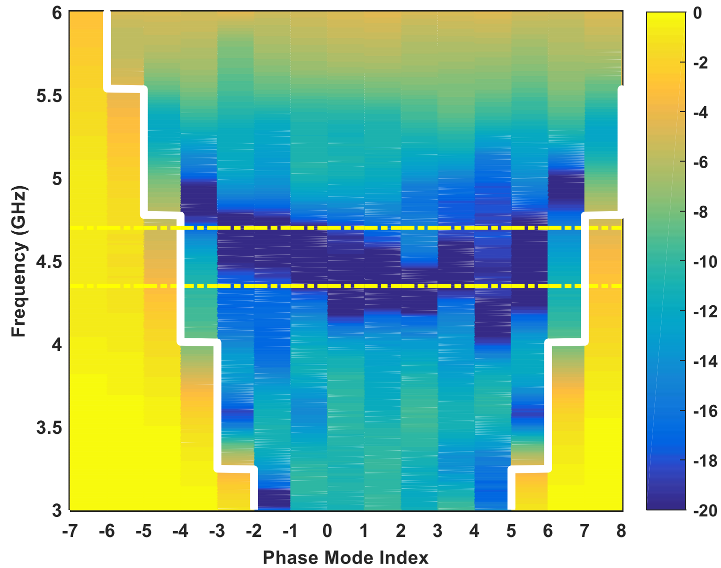

Figure 23: Active reflection coefficient plotted with varying frequency and phase modes

The equalization errors are shown in Figure 24. Equalization errors are phase corrections that have to be applied at each of the Butler matrix outputs to ensure that the phases of all phase modes are coincident.

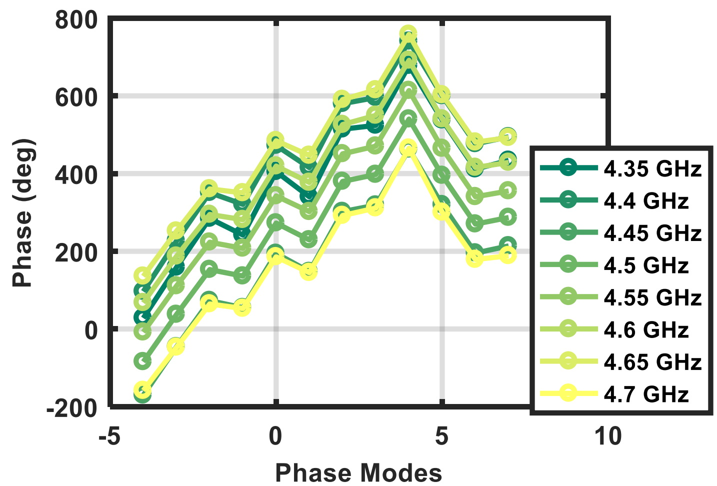

Figure 24: Phase corrections to obtain equalization between the phase modes

After equalization, the phase modes can be summed to obtain the overall radiation pattern as shown in Figure 25. Note that equalization results in a frequency invariant directional pattern. The beamwidth across the 4.35 – 4.75 GHz bandwidth is equal. In each case, only 12 phase modes are used to form the beam shown in Figure 23.

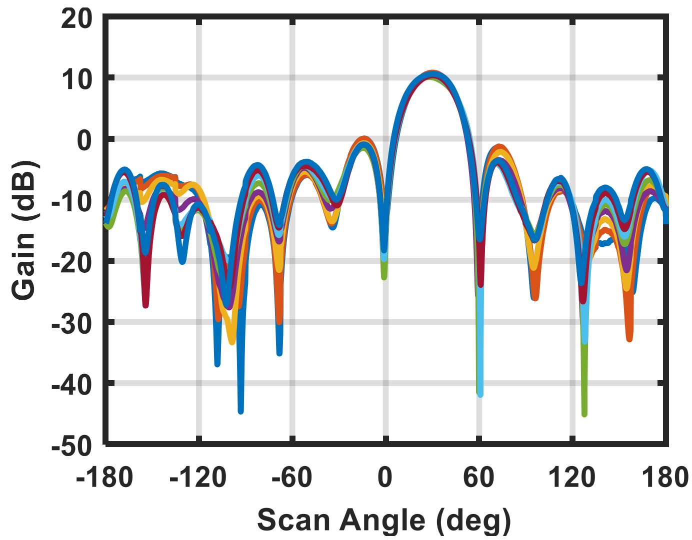

Figure 25: Directional beam obtained by combining the equalized phase modes. The directional beam is pointing at 45 deg.

Finally, Figure 26 shows how summing the un-equalized phase modes allows us to calculate the embedded element pattern. However, errors in the hardware affects the calculation of the overall embedded element pattern as shown in Figure 26. This pattern is only shown for the case of 4.5 GHz. In the next section, we discuss the development of a test-bed designed to set up and measure the different parts of the Butler matrix.

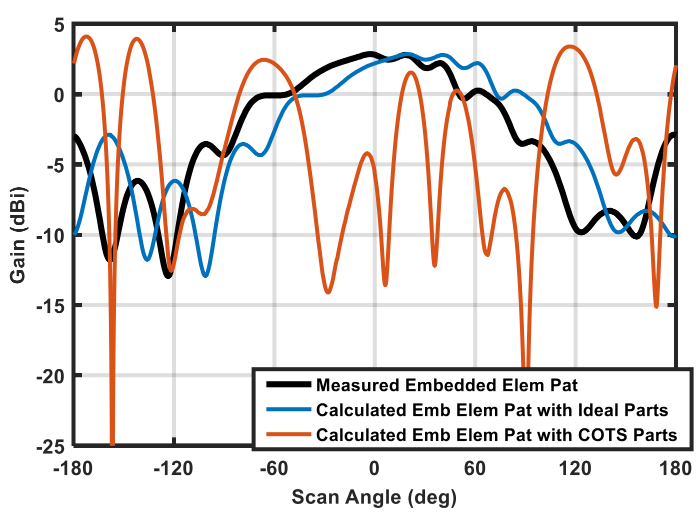

Figure 26: Measured and calculated embedded element pattern

5. TEST BED DEVELOPMENT

For the next steps, the plan is to build a 4-port Butler matrix in hardware and measure it's S-parameters and then grow this design to a full 16-port Butler matrix to operate over wider bandwidths.

In order to characterize each of the 180^{o} surface mount hybrids purchased from Werlatone, it was necessary to develop a test fixture comprised of two parts. The first is the mechanical holder used to hold and align the hybrid part during the testing. The second is the circuit board that will provide the RF connection to the hybrid. The mechanical holder also includes an RF path from the circuit board to the hybrid. Figure 27 shows the overview of the holder assembly.

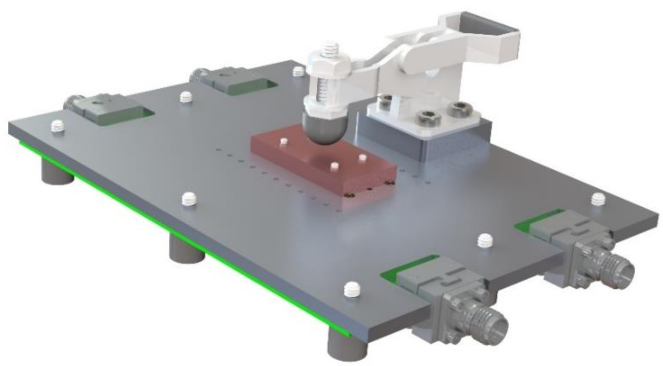

Figure 27: Test fixture to characterize the 180deg surface mounts

The device under test (DUT) is the Werlatone model H10126 180^{o} hybrid whose performance is shown in Figure 10. The DUT is approximately 0.1" X 0.6" X 0.1" and uses the four ports as shown in Figure 9. These four ports are located at the corners of the device. To enable the test fixture to measure the DUT in a non-destructive manner, the fixture utilizes a pogo pin shown in Figure 28. A pogo pin, also known as a spring-loaded pin, is a type of electrical connector mechanism that is often used for testing purposes. In this test fixture, the pogo pin provides an RF path to the DUT without requiring it to be soldered to the device. The top section of the pin compresses into the body while still maintaining RF connectivity across the pin. The length of the pin is approximately 0.14 inches in length and 0.04 inches in diameter and it is attached to the circuit board as shown in Figure 29

Figure 28: Pogo pin

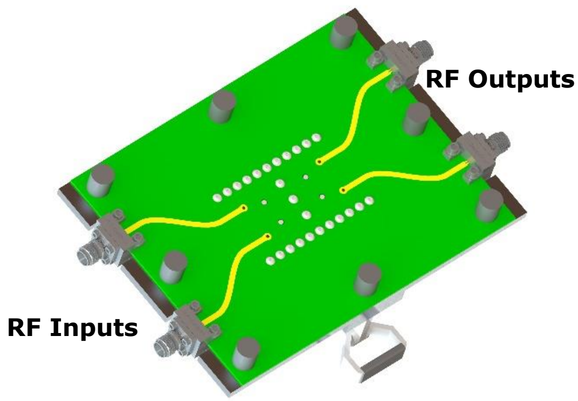

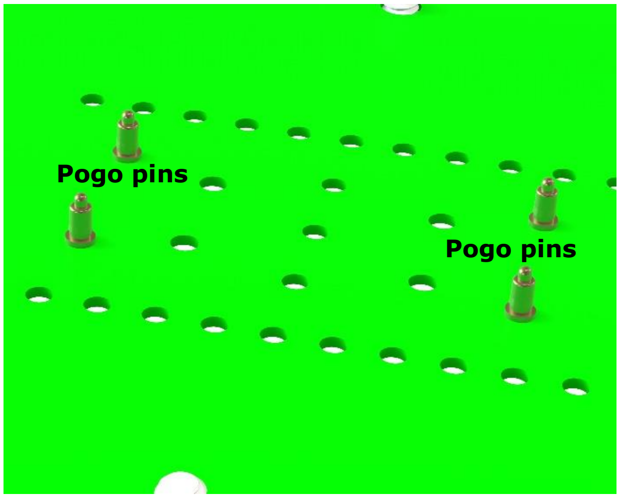

(a) (b)

Figure 29: (a) Top side of circuit board and (b) bottom side of circuit board

In order to maintain the 50Ω impedance that is provided by the microstrip line up to the hybrid connection point, the pogo pin acts like the center conductor of a coaxial cable. Additionally, the diameters of the feed-thru holes are designed based on the formula for a standard coaxial structure as shown in Eq. (18). Knowing the center conductor diameter, D_{center}, the outer diameter of the coaxial can be calculated from the formula for a 50 Ω impedance.

$$D_{outer} = D_{center} \times 10^{(0.362 \times \sqrt{e_r})} \tag{18}$$

In Eq. (18) the parameter, e_r, is the dielectric constant of the material between the center and outer conductors. A cross-section of the pin and plate is shown in Figure 30. Table 4 gives the details of design.

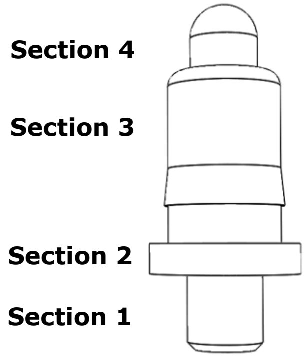

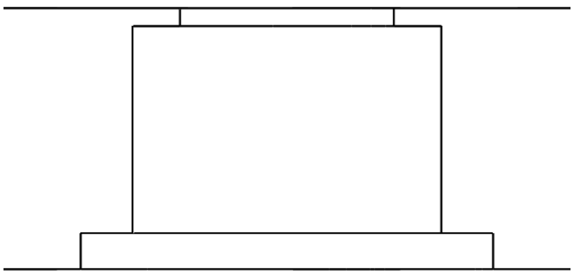

(a) (b)

Figure 30: (a) Pogo pin outline with the 4 sections and (b) Feed-thru outline in the fixture

Table 4: Inner and outer diameters for the coaxial cable feed-thrus

	Diameter (inches)	
	Pogo Pin (inner conductor)	**Test Fixture (outer conductor)**
Section 1 Circuit Board, $e_r = 3.66$	0.0393	0.1939
Section 2 Test Fixture, $e_r = 1$	0.0787	0.1812
Section 3 Test Fixture, $e_r = 1$	0.0591	0.1359
Section 4 Test Fixture, $e_r = 1$	0.0354	0.0815

Since part of the pin is located in the circuit board, the outer wall of the coaxial structure is made by a series of vias placed on a circular pattern as shown in Figure 31. This is done to maintain the 50 Ω impedance.

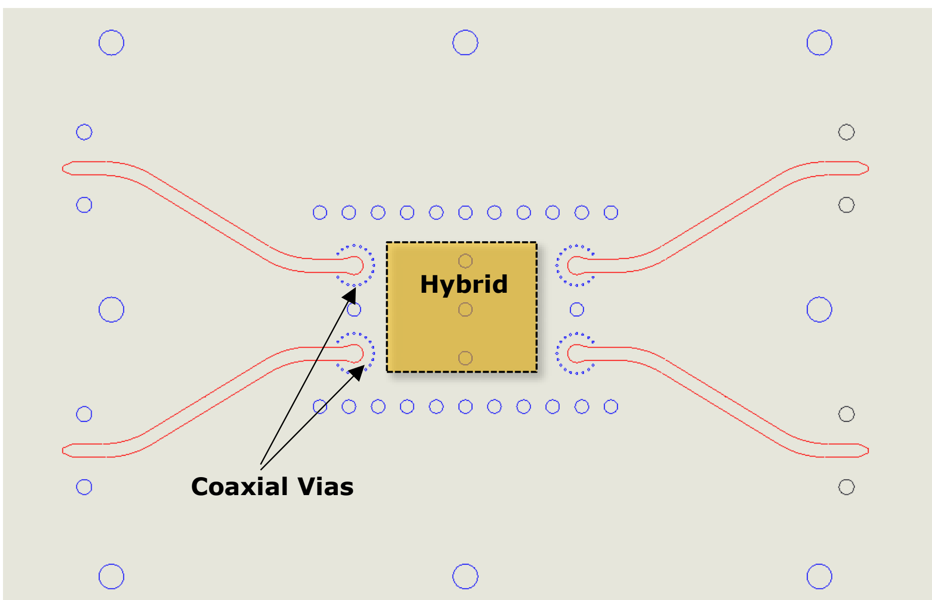

Figure 31: Top layer of the circuit board

To verify the performance of the circuit board and pogo pin interface, an electromagnetic (EM) model of the assembly was generated in FEKO [12]. FEKO is a Method of Moments code that is used to model antenna and circuit structures. Figure 32 shows the layout of a single trace associated with the test assembly. The Voltage Standing Wave Ratio (VSWR) of the test assembly is shown in Figure 33 and the input impedance represented on a Smith chart is displayed in Figure 34. The results show that there is some reactance associated with this structure and will need to be further investigated to understand the causes of this reactance and how to mitigate it.

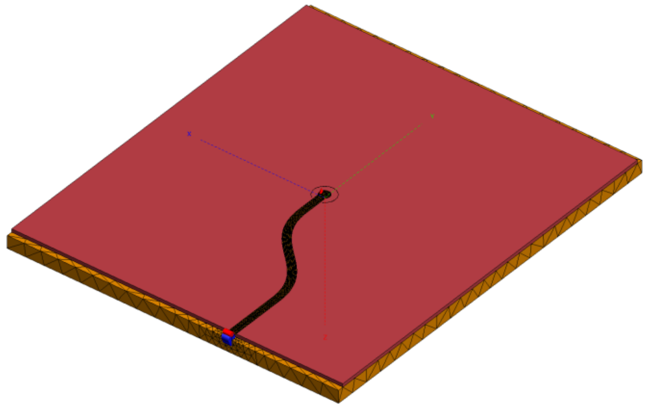

Figure 32: Single trace microstrip to pogo feed-thru

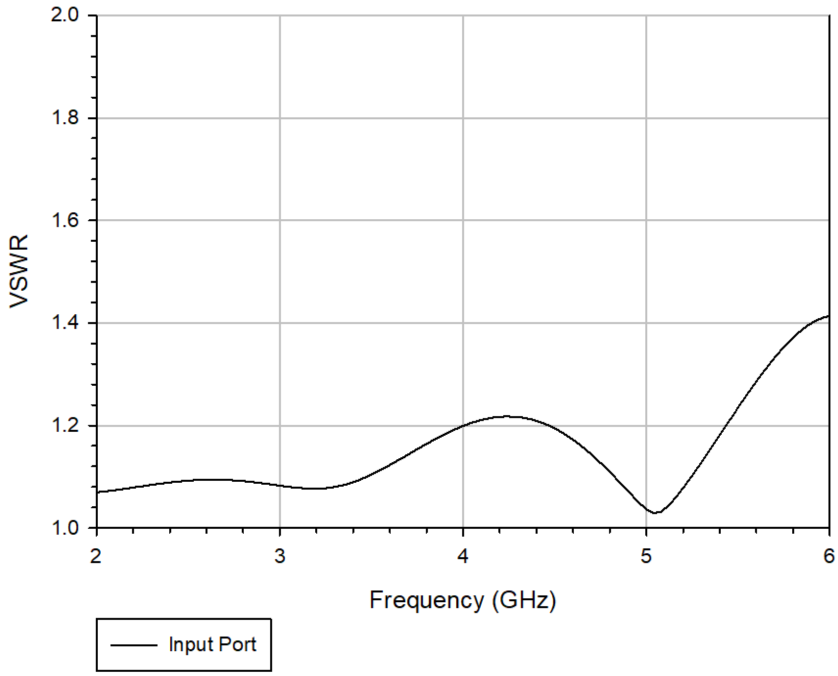

Figure 33: VSWR of input port trace (50 ohm terminated)

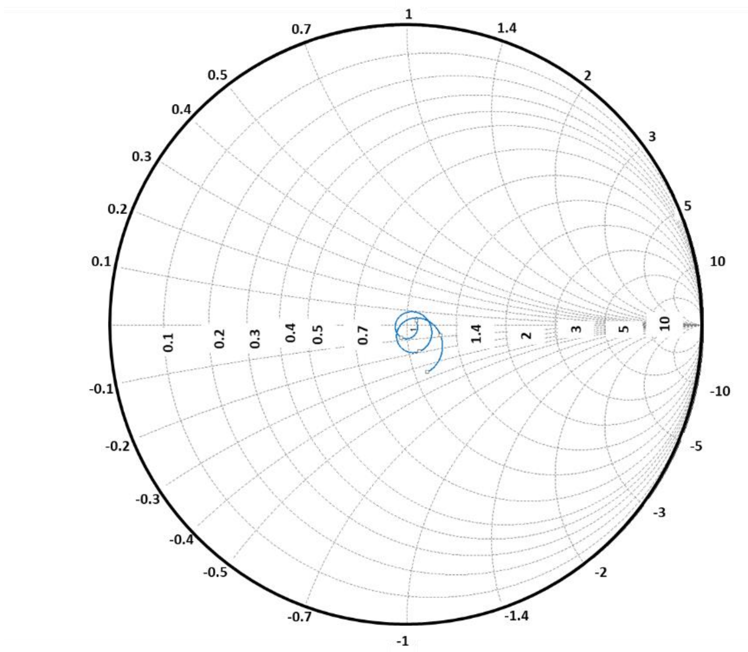

Figure 34: Smith chart representation of the input impedance

5.1 4 X 4 Beamformer Design

Once these hybrids are fully characterized, the data will be used to start the design of the 4×4 beamforming network. In order to remove the cross-over needed, as shown in Figure 35, the hybrids are placed on a circular arc, shown in Figure 35a, which removes the need for cross-overs but now places some of the input and output ports in the center of the circle, where they will be hard to access. Since the design of a hybrid is such that each port can be accessed from either side, the hybrids can be configured such that the ports that are on the inside of the circle can be placed on the outside by simply flipping the hybrids. Figure 35b shows that by flipping hybrids 3 and 4 all of the hybrid ports now reside on the outside of the circle and we have also managed to get rid of the need for any cross-overs.

When designing the 90^{o} phase shift circuit, stripline techniques can help improve the bandwidth performance of this structure over conventional microstrip techniques due to the wideband characteristics of the even- and odd-impedances associated with coupled lines. A conceptual design for the full 4×4 beamformer is shown in Figure 36a. In this layout all the reference and phase shift lines will be constructed using stripline techniques, as shown in Figure 36b, while the input and output from the beamformer will use microstrip lines. When constructing the final 16×16 port beamformer the new construction techniques will be used where possible. Details of the design will be discussed in a future report.

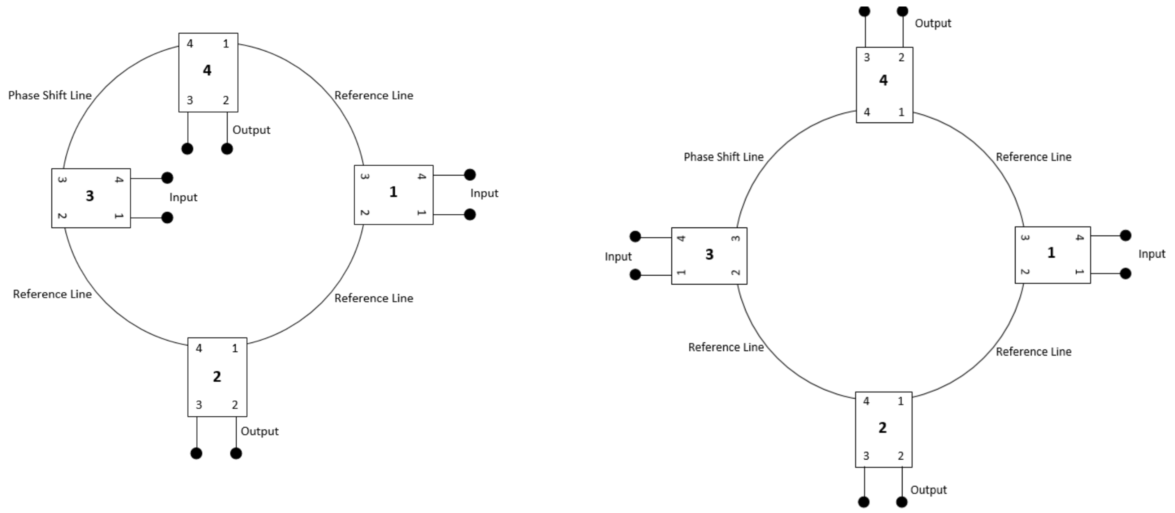

(a) Original Layout (b) Flipped Design

Figure 35: 4 × 4 Beamformer layout configurations

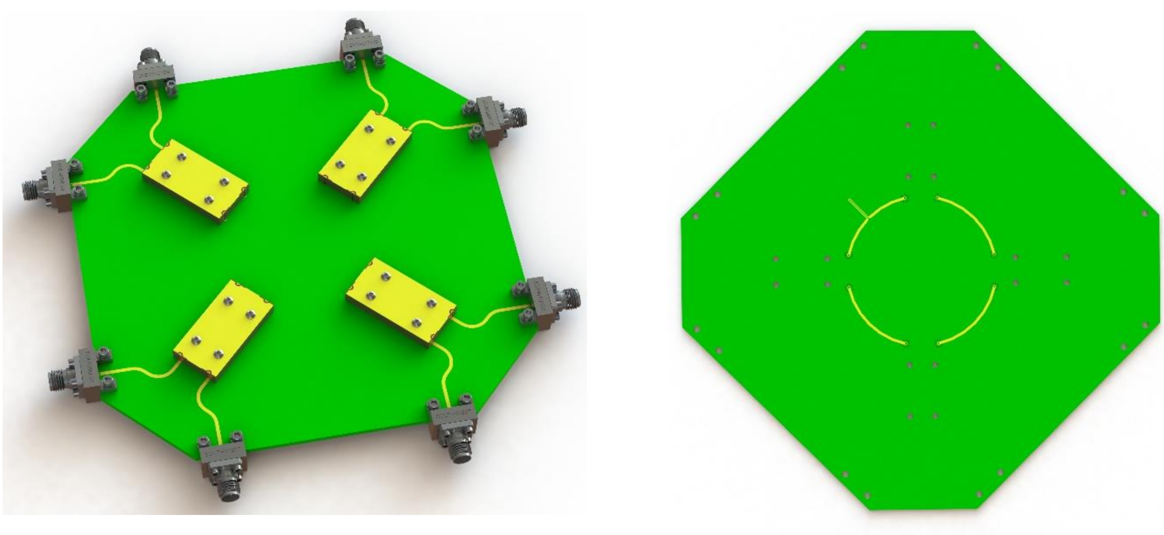

(a) Top layer using microstrip design (b) Middle layer using stripline design

Figure 36: 4 × 4 beamformer assembly

6. SUMMARY

In this report, we have provided an overview of circular array beamforming using the concept of phase modes. The use of phase modes allows circular arrays to be presented analogous to linear arrays. Once this transformation has taken place, it is possible to implement mature linear array beamforming techniques to obtain directional beams as well as carry out nulling techniques to improve interference mitigation and isolation. We have provided insight into why Butler Matrices are appropriate networks that can be used to generate these phase modes and presented equalization errors that can be generated due to non-ideal hardware.

At present we are in the process of designing and building a test bed that we can utilize to measure the S-parameters of the 180 deg hybrids. A short overview of this test bed has been discussed. Future work will include building a small 4×4 butler matrix whose measured performance will be compared against the modeled performance to better understand errors incurred in the modal beamformer and how these have to be compensated for the generation of directional beams.

7. BIBLIOGRAPHY

[1] G. V. Trunk and D. P. Patel, "Optimal number of phased array faces for horizon surveillance," in *IEEE International Symposium on Phased Array Systems and Technology*, Boston, MA, 1996.

[2] G. Galati, F. Madia, P. Carta, E. G. Piracci, R. Stallone and M. Massardo, "Time for a change in phased array radar architectures -- part I: Planar vs. conformal arrays," in *2015 16th International Radar Symposium* , Dresden, 2015.

[3] H. Steyskal, "Digital beamforming aspects of wideband circular arrays," in *2008 IEEE Aerospace Conference*, Big Sky, MT, 2008.

[4] T. Rahim and D. E. N. Davies, "Effect of directional elements on the directional response of circular antenna arrays," *IEE Proceedings,* vol. 129, no. 1, 1982.

[5] S. Vashist, M. K. Soni and P. K. Singhal, "A Review on the development of Rotman Lens Antenna," *Chinese Journal of Engineering,* vol. 2014, 2014.

[6] L. Josefsson and P. Persson, Conformal Array Antenna Theory and Design, John Wiley & Sons, 2006.

[7] B. Shelag, "Butler submatrix feed systems for antenna arrays," *IEEE Transactions on Antennas and Propagation,* vol. 21, no. 2, pp. 228-229, 1973.

[8] T. Macnamara, "Simplified design procedures for Bulter matrices incorporating 90deg hybrids or 180 deg hybrids," *IEE Proceedings,* vol. 134, no. 1, 1987.

[9] W. M. Dorsey, A. Stumme, K. M. Charipar and N. A. Charipar, "3-D Printed Circular Array for WiMAX Base Station," *IEEE Antennas and Wireless Propagation Letters,* vol. 18, no. 6, pp. 1159 - 1163, 2019.

[10] W. M. Dorsey, R. Mital, W. R. Pickles, D. P. Patel, J. Valenzi, A. Stumme and J. O. Coleman, "Design of a Wideband Dual-Polarized Circular Array," US Naval Research Lab, Washington, DC, 2018.

[11] C. J. Fulton and A. Mirkamali, "A computer-aided technique for the analysis of embedded element patterns of cylindrical arrays[EM programmer's notebook]," *IEEE Antennas and Propagation Magazine*, vol. 57, no. 3, pp. 132-138, 2015.

[12] AltairHyperWorks, "Altair Feko Overview," [Online]. Available: https://altairhyperworks.com/product/Feko.